Published in final edited form as:
IEEE Trans Nanobioscience. 2008 September ; 7(3): 223. doi:10.1109/TNB.2008.2002288.

Magnetically Targeted Viral Envelopes: A PET Investigation of Initial Biodistribution

Jennifer A. Flexman,
Department of Bioengineering, University of Washington, Seattle, WA 98195-5061 USA

Donna J. Cross,
Department of Radiology and Washington National Primate Research Center, University of Washington, Seattle, WA 98195-5061 USA, and also with the Neuroscience Graduate Program, University of Michigan, Ann Arbor, MI 48109-2215 USA

Barbara L. Lewellen,
Department of Radiology, University of Washington, Seattle, WA 98195-5061 USA

Sosuke Miyoshi,
Department of Bioengineering, University of Washington, Seattle, WA 98195-5061 USA. He is now with Astellas Pharma, Inc., Tsukuba 305-8585, Japan

Yongmin Kim [Fellow, IEEE], and
Department of Radiology and the Department of Bioengineering, University of Washington, Seattle, WA 98195-5061 USA

Satoshi Minoshima
Department of Bioengineering, the Department of Radiology, and the Washington National Primate Research Center, University of Washington, Seattle, WA 98195-5061 USA

Jennifer A. Flexman: ; Donna J. Cross: ; Barbara L. Lewellen: ; Sosuke Miyoshi: ; Yongmin Kim: ; Satoshi Minoshima: minoshim@u.washington.edu

Abstract

Gene and drug therapy for organ-specific diseases in part depends on the efficient delivery to a particular region of the body. We examined the biodistribution of a viral envelope commonly used as a nanoscale gene delivery vehicle using positron emission tomography (PET) and investigated the magnetic alteration of its biodistribution. Iron oxide nanoparticles and ^{18} F-fluoride were encapsulated by hemagglutinating virus of Japan envelopes (HVJ-Es). HVJ-Es were then injected intravenously in the rat and imaged dynamically using high-resolution PET. Control subjects received injections of encapsulated materials alone. For magnetic targeting, permanent magnets were fixed on the head during the scan. Based on the quantitative analysis of PET images, HVJ-Es accumulated in the liver and spleen and activity remained higher than control subjects for 2 h. Histological sections of the liver confirmed imaging findings. Pixel-wise activity patterns on coregistered PET images of the head showed a significantly different pattern for the subjects receiving magnetic targeting as compared to all control groups. Imaging demonstrated the initial biodistribution of a viral envelope within the rodent by providing quantitative behavior over time and in specific anatomical regions. Magnetic force altered the biodistribution of the viral envelope to a target structure, and could enable region-specific delivery of therapeutic vehicles noninvasively.

Correspondence to: Satoshi Minoshima, minoshim@u.washington.edu.

Index Terms

Biomagnetics; biomedical imaging; biomedical nuclear imaging; nanotechnology; paramagnetic materials

I. Introduction

Viral vehicles have been investigated for the delivery of genes *in vivo* due to their innate ability to fuse with cellular membranes and consequential high efficiency of delivery of genetic material. One of the challenges has been to target therapeutic gene carriers to certain regions of the body and to permit subsequent transfection so that the administration of large doses of viral material or transfection in nontarget organs can be avoided [1]–[3].

The optimization of gene therapy involves several critical steps, including the efficiency of the delivery vehicle to reach the target area or cells. While many research studies have investigated the latter stage of gene vectors and their expressions *in vivo*, such as through reporter genes, limited research has been done to determine the initial biodistribution of the delivery vehicle itself. A method of monitoring the behavior of viral vehicles *in vivo* after intravenous injection will improve the design of new technologies to circumvent the limitations of clearance and the evaluation of targeting strategies. This method must be dynamic, sensitive, and quantitative to ensure objective comparisons over time. The versatile characteristic of a viral envelope is critical because it enables the coencapsulation of multiple nanoscale materials for multimodality imaging, therapy, and targeting.

The hemagglutinating virus of Japan (HVJ) has been used effectively in gene therapy both as a reconstituted envelope and fused with liposomes. It has a high transfection efficiency for many cell types, particularly cells of the central nervous system, as well as a versatility in encapsulating various molecular subtypes such as proteins [4], [5]. The reconstituted HVJ envelope (HVJ-E) has been shown to efficiently transfect neural progenitor cells with superparamagnetic iron oxide (SPIO) containing ferumoxide particles for cell tracking with MRI [6]. We hypothesized that the versatility of HVJ-Es would enable the encapsulation of multiple agents chosen for maximum radiotracer encapsulation and magnetic targeting.

SPIO nanoparticles have generated interest for their properties both in targeting and MRI, and for their lack of toxicity in the body [7]. Commercial cell sorting systems take advantage of the affinity SPIO particles have for uniform magnetic fields, and *in vivo* targeted delivery techniques have shown that the therapy can be delivered more efficiently to a specific region of the body using magnetic attraction [8]–[12]. HVJ-Es have been associated with magnetic nanoparticles using surface modifications to enhance gene transfection efficiency, but this model has not been tested *in vivo* after intravenous administration using magnetic targeting [13]. The targeting of a systemic delivery vehicle encapsulating magnetic nanoparticles could potentially open new doors for the delivery of genes and drugs to the cerebral vasculature after trauma or for the treatment of brain disease.

Positron emission tomography (PET) is an imaging technique that is sensitive to the detection of radiotracers within the body and can provide longitudinal imaging over the lifetime of the radiotracer. Because the detected radioactivity by PET imaging is proportional to the concentration of the radiotracer, images can be quantified to give objective measures of biodistribution *in vivo*. Radioactive fluorine (^{18}F-fluoride) is a positron emitter with a half-life of 110 min, allowing a sufficient window of observation for initial biodistribution. For example, ^{18}F-fluoride has been shown to adequately label dendritic cells prior to transplantation for *in vivo* PET imaging of cellular migration and distribution in mice [2].

Moreover, the radiotracer ^{18}F-fluoride is cleared from the bloodstream to the bones and excreted by the kidney and has minimal specific soft tissue uptake [14]. This is important in soft tissues for distinguishing between ^{18}F-fluoride activity detected from within a delivery vehicle and unencapsulated ^{18}F-fluoride, which may have leaked from the vehicle membrane. However, a versatile method is needed to incorporate a radioactive ion within a viral envelope.

Recently, PET imaging has been used to visualize gene expression *in vivo* through the addition of reporter genes that can selectively express elements required for radiotracer binding or transport into the cell. For example, the herpes simplex virus type 1 thymidine kinase gene (HSV1-tk) acts as a reporter gene by resulting in the phosphorylation of certain radioactive probes and subsequent accumulation of these probes in transfected cells [15]. The HSV1-tk reporter system for PET has been used to demonstrate transgene expression in multiple tissues, including the heart and prostate [16], [17]. These methods represent an effective technique for visualizing, and ultimately, quantifying gene expression for therapy. However, they do not address the pharmacokinetics of initial clearance and targeting efficiency of the nanoscale delivery vehicle itself. The *in vivo* characterization of the biodistribution of the delivery vehicle is essential to the development and clinical translation of systemic gene and nanocarrier-mediated drug therapy.

Previously, we demonstrated the feasibility of PET imaging to visualize the HVJ-E after radioactive tagging [18]. In this study, we investigated the biodistribution of HVJ-Es *in vivo* in the rat by incorporating both ^{18}F-fluoride for PET and SPIO nanoparticles (ferumoxides) for targeting. Magnetic targeting was evaluated by examining at the initial biodistribution on PET of tagged HVJ-Es in the presence of multiple permanent magnets fixed *ex vivo* to the top of the head. The encapsulation of ^{18}F-fluoride by HVJ-Es was optimized using ferumoxides and other cationic agents because of leakiness due to the low molecular weight of ^{18}F-fluoride. The distribution of radioactively tagged HVJ-Es was evaluated quantitatively and over time in the liver, kidney, and spleen and imaging findings were compared with histology. Spatial distribution patterns of HVJ-Es in the head were examined after magnetic targeting.

II. Materials and Methods

A. HVJ-E Encapsulation of ^{18}F-Fluoride and Ferumoxides

HVJ-Es (GenomeOne, Ishihara Sangyo, Osaka, Japan) reconstituted from HVJ membrane proteins are approximately 300 nm in diameter and were used to encapsulate imaging and targeting agents as previously described [18]. ^{18}F-fluoride (approximately 18.5 MBq/μL) in solution and one of either phosphate-buffered saline (PBS) or SPIO-containing ferumoxides (Feridex IV; Berlex Laboratories, Wayne, NJ; approximately 150 nm in diameter) at 11.2 mg of iron per milliliter was mixed in equal parts (total volume of 120 μL) with the equivalent of HVJ-Es required to transfect 10^6 cells. A detergent supplied by the manufacturer was added to open the membrane and allow ^{18}F-fluoride and ferumoxide solutions to penetrate HVJ-Es. HVJ-Es were washed twice and suspended in 400 μL of PBS. All steps were performed at 4 °C. Radioactivity corresponding to encapsulated ^{18}F-fluoride was measured on a Packard COBRA gamma counter (PerkinElmer, Boston, MA). Decay-corrected readings were used to calculate the encapsulation efficiency based on added radioactivity.

B. HVJ-E Encapsulation Using Cationic Agents

Initial experimental results demonstrated that ^{18}F-fluoride encapsulation efficiency was compromised due to ions leaking from the viral membrane. To improve the encapsulation efficiency, ^{18}F-fluoride ions in suspension were combined with various synthetic cationic polypeptides (1 mg/mL) in a ratio of 2:1 in PBS and left to form complexes at 4 °C for 10 min. Peptides consisted of one of Lipofectamine 2000 (L2000; Invitrogen, Carlsbad, CA) or poly-

L-lysine (PLL) of molecular weight (MW) 9.2, 66.7, or 574.5 kDa (Sigma Aldrich, St. Louis, MO). ^{18}F-fluoride-peptide complexes and PBS in a ratio of 3:1 (total volume of 120 μL) or ^{18}F-fluoride-peptide complexes and ferumoxide solution (11.2 mg of iron per milliliter) in a ratio of 3:2 (total volume of 150 μL) were mixed with HVJ-Es and processed as described in the previous section.

C. Positron Emission Tomography

To investigate the initial biodistribution of HVJ-Es encapsulating a radiotracer, PET imaging was performed after systemic injection. The University of Washington Institutional Animal Care and Use Committee approved all animal procedures, following guidelines established by the United States National Institutes of Health. Thirteen male Sprague Dawley rats (100–150 g) anesthetized with 2% isoflurane gas received tail injections of either HVJ-Es or control materials without HVJ-Es consisting of combinations of PLL, ferumoxides, and ^{18}F-fluoride. The injection groups consisted of 0.56–0.93 MBq of one of: 1) HVJ-Es containing ^{18}F-fluoride, PLL (MW 66.7 kDa), and ferumoxides (HVJ-E, n = 3); 2) HVJ-Es as described with a magnet taped to the head (HVJ-E MAGNET, n = 3); 3) ^{18}F-fluoride-PLL-ferumoxide complexes (C-FPF, n = 3); 4) ^{18}F-fluoride-PLL complexes (C-FP, n = 4); or 5) ^{18}F-fluoride alone (C-F, n = 5). Five animals injected in the HVJ-E, HVJ-E MAGNET, or C-FPF groups were subsequently used in the C-FP or C-F groups after 24 h after radioactive decay. Whole body imaging (dynamic, 2-D, 39 frames, 120 min) was performed on a dedicated animal PET scanner (SHR-7700, Hamamatsu Photonics K.K., Hamamatsu, Japan). Decay-corrected images were reconstructed using a filtered backprojection method to in-plane pixel sizes of 0.3 mm and a slice thickness of 3.6 mm, resulting in a reconstructed in-plane spatial resolution of approximately 2.4 mm full-width at half-maximum at the center of the field of view.

D. Magnetic Targeting of HVJ-Es to the Head

To test the feasibility of magnetically targeting HVJ-Es encapsulating SPIO particles, permanent magnets were applied to the top of the head. Five 1.04 tesla (T) neodynium (NdFeB) permanent magnets (Culver City Industrial Hardware, Culver City, CA) 1.3 cm in diameter and 0.15 cm thick were taped externally to the center of the top of the head for the duration of the scanning session. The magnetic flux density of the ensemble of magnets was plotted for a grid of points (0, 3, 6, 9, and 12 mm from the center of the magnets and 0–10 mm above the surface of the magnets in 1-mm increments) using a gaussmeter (model 410-SCA, Lake Shore Cryotronics, Inc., Westerville, OH) clamped in a stereotaxic holder. To confirm that the ensemble of magnets was capable of exerting a magnetic force on the SPIO particles, the magnets were placed below a polystyrene dish (approximately 1 mm in thickness) containing ferumoxides at 1.12 mg of iron per milliliter and digital images were acquired before and after magnet placement (Canon Powershot SD110; Canon USA, Inc., Lake Success, NY).

E. Histology

Because iron contained within ferumoxides acts as a biomarker of HVJ-Es, tissues were harvested for Prussian blue staining. One subject for each group received a tail vein injection and tissues were harvested at 120 min postinjection, preserved in 10% formalin and processed for staining. Comparisons with control groups estimated staining due to endogenous iron. Tissues consisted of the liver and spine, including the spinal cord. Tissues were stained for Prussian blue using equal amounts of 2% potassium ferrocyanide in 2% hydrochloric acid solution and were counterstained with nuclear fast red. The bone specimens were demineralized prior to staining. Photographs were taken of representative fields using an upright, light microscope (Nikon Eclipse; Nikon, Tokyo, Japan), and 1360 × 1036 pixel, 24-bit camera control driver (CCD) digital camera (QImaging, Burnaby, BC, Canada).

F. Image Analysis

The liver, kidneys, and spleen were investigated using region of interest (ROI) analysis of time-averaged activity. To normalize activity levels due to inconsistencies in radioactive dose and because unencapsulated ^{18}F-fluoride is cleared to the bones [14], liver, kidney, and spleen uptake were normalization to bone activity in the posterior spine. Specifically, average uptake in three circular liver ROIs (5.72 mm^2 each), two circular spleen ROIs (1.77 mm^2 each), and one circular kidney ROI (1.77 mm^2 each) were normalized by the average steady-state (90–120 min) uptake in three circular posterior spine ROIs (1.77 mm^2 each) on transaxial slices. To avoid overlap with the liver, only the left kidney was investigated. Two subjects (one from HVJ-E group and one from C-F group) were not included in the kidney analysis because the left kidney could not be identified clearly on PET images. Uptake over the first 10 min was discarded to avoid individual differences due to injection rate. Dynamic activity corresponding to ROI analysis on each time frame was plotted for the liver and spleen and normalized by the average steady-state uptake in the posterior spine. Representative images were created as coronal projections of the average, normalized activity in the whole body of representative subjects from 10 to 30 min, 30 min to 1 h, and 1 to 2 h. In addition, single-slice, transaxial images of average, normalized activity in the liver and spleen were generated for representative subjects from 10 to 30 min.

Head regions of the whole-body images were trimmed and coregistered using automatic rigid-body transformation prior to ROI analysis (NEUROSTAT, University of Washington). The algorithm uses mutual information [19] as a cost function and Powell's iterative search algorithm to optimize six parameters (x–y–z translation and rotation) [20]. Uptake in the brain was normalized by the average steady-state (90–120 min) uptake in the skull (the same three-circular ROIs of 1.77 mm^2 on registered images). Time points less than 10 min were discarded to avoid differences due to injection rate. Registered and normalized images within each group were averaged on a pixel-wise basis. The percent difference of the HVJ-E and control group activity as compared to the HVJ-E MAGNET group activity, normalized to the HVJ-E MAGNET group activity, was calculated for each pixel to demonstrate spatial distribution of magnetically targeted activity. For a percent difference greater than 10% as compared to HVJ-E MAGNET, the activity ratio of the pixel area of the decreased activity to the pixel area of the increased activity for each group (HVJ-E, C-FPF, C-FP, and C-F) was calculated as

$$\text{Activity ratio} = \frac{\text{number of pixels } (>10\% \text{ decrease})}{\text{number of pixels } (>10\% \text{ increase})}. \quad (1)$$

G. Statistical Analysis

For analysis of encapsulation efficiencies, average uptake values and early and late mean uptake values for dynamic imaging, statistical significance was determined using the student's t-test for independent samples with significance at $p < 0.05$. In the head, the dataset of pixels for each subject was reduced by a factor of 24 by calculating the average activity in squares of 25×25 pixels on each frame. Analysis of variance (ANOVA) analysis was done on the reduced dataset between the groups after adjusting for repeated measures with significance at $p < 0.05$. This analysis was repeated for differently sized data reduction blocks and yielded the same outcome.

III. Results

A. HVJ-E Encapsulation Using Ferumoxides and Cationic Agents

Coencapsulation with ferumoxides resulted in a greater uptake of ^{18}F-fluoride by HVJ-Es, and increased the encapsulation efficiency of ^{18}F-fluoride by 4.7 ± 0.5 times (white bar, Fig. 1). HVJ-Es encapsulated ^{18}F-fluoride in combination with ferumoxides with an efficiency of 0.0378% ± 0.0027%, which was significantly different from the encapsulation of ^{18}F-fluoride alone, which had an efficiency of 0.0080% ± 0.0007% ($p < 0.01$). The absolute numbers of encapsulation efficiency were small in part since the HVJ-E encapsulation was carried out in an aliquot in which the total physical volume of HVJ-E particles was relatively small compared to the total volume of the aliquot.

Cationic agents were effective in significantly increasing the encapsulation efficiency of ^{18}F-fluoride by HVJ-Es as compared to ^{18}F-fluoride alone in the presence of ferumoxides (Fig. 1). Lipofectamine 2000, PLL (MW 9.2 kDa), PLL (MW 66.7 kDa), and PLL (MW 574.5 kDa) in combination with ferumoxides resulted in an encapsulation efficiency of ^{18}F-fluoride of 0.1152% ± 0.0220%, 0.0859% ± 0.0126%, 0.1507% ± 0.0242%, and 0.1306% ±0.0093%, respectively. PLL (MW 66.7 kDa) demonstrated the highest overall ^{18}F-fluoride encapsulation efficiency, which was significantly greater than PLL (MW 9.2 kDa) but not PLL (MW 574.5 kDa) or Lipofectamine 2000. All cationic peptides resulted in significantly higher encapsulation efficiency in combination with ferumoxides than without ($p < 0.01$; Fig. 1). Without Feridex, Lipofectamine 2000, PLL (MW 9.2 kDa), PLL (MW 66.7 kDa), and PLL (MW 574.5 kDa) resulted in an encapsulation efficiency of ^{18}F-fluoride of 0.0098% ± 0.0014%, 0.0046% ± 0.0003%, 0.0138% ± 0.0008%, and 0.0150% ± 0.0090%, respectively.

B. HVJ-E Uptake in the Liver, Kidney, and Spleen

Coronal projections of average pixel intensities in different time blocks of whole body scans demonstrated an accumulation of ^{18}F-fluoride in the bones as early at 30 min for all subjects, but only those subjects that received injections of HVJ-Es showed early (10–30 min) liver and spleen activity (see Fig. 2). Fig. 3 demonstrates that the normalized, average signal intensity in the liver for the subjects receiving HVJ-Es was significantly greater than the activity of all control groups from 10 to 30 min ($p < 0.05$), 30 min to 1 h ($p < 0.05$), and 1 to 2 h ($p < 0.01$). Similarly, Fig. 3 also shows that the normalized, average signal intensity in the spleen was significantly greater for the subjects receiving HVJ-Es than control subjects from 10 to 30 min ($p < 0.05$), 30 min to 1 h ($p < 0.05$), and 1 to 2 h ($p < 0.05$). In the kidney, there was no significant differences between the groups except that the C-FP group showed greater normalized activity from 10 to 30 min than the HVJ-E group ($p < 0.05$; Fig. 3).

The difference in activity distribution was shown in transaxial slices as well, where HVJ-Es showed greater activity in the liver [Fig. 4(a)] and spleen [Fig. 4(b)] as compared to all subjects who received control materials. The uptake of activity for HVJ-Es in the liver [Fig. 4(c)] and spleen [Fig 4(d)] after normalization to the steady-state activity in the posterior spine remains higher than all control subjects for every time point and decreased with time.

C. Histology

Prussian blue staining of liver slices revealed areas in the tissue with iron deposits corresponding to SPIO particles under light microscopy (Fig. 5). Blue areas, indicating ferumoxides particles encapsulated within HVJ-Es, were detected in HVJ-E and HVJ-E MAGNET subjects. The C-FPF subjects, which received PLL-^{18}F-fluoride in combination with ferumoxides, also showed iron deposits in the liver. No apparent iron staining was seen for the C-FP and C-F subjects. No apparent iron staining was found in the bone or bone marrow in any subjects.

D. In Vitro Magnetization of Ferumoxides

The magnetic flux density profile of the ensemble of permanent magnets decreased with distance from the magnets, and had a peak of 352 mT [see Fig. 6(a)]. When the permanent magnets were applied to polystyrene dish containing ferumoxides at 1.12 mg of iron per milliliter suspended in PBS [see Fig. 6(b)], after 1 h, the aggregation of the particles is visible as a ring around the inner diameter of the magnets [see Fig. 6(c)].

E. HVJ-E Uptake in the Head Region

The application of permanent magnets to the top of the head [see Fig. 6(d)] resulted in a significantly different uptake pattern in the head for HVJ-E MAGNET subjects as compared to HVJ-E without magnet subjects, and as compared to all control subjects based on ANOVA results ($p < 0.00001$). There was no significant difference between uptake patterns for HVJ-E without magnet subjects as compared to all control subjects, and between any control groups. The coregistered images are shown in Fig. 7, where group-averaged pixels with over 10% *less* activity than HVJ-E MAGNET subjects are shown in color. Coregistered group-averaged pixels with over 10% *greater* activity than HVJ-E MAGNET subjects are shown in Fig. 8. The HVJ-E MAGNET group demonstrated a greater proportion of pixels with a greater than 10% increase in the activity than a greater than 10% decrease in the activity as compared to HVJ-E and control groups. The activity ratio of the pixel area of the decreased activity to the pixel area of the increased activity was 0.51, 0.54, 0.19, and 0.18 for HJV-E, C-FPF, C-FP, and C-F, respectively, as compared to HVJ-E MAGNET for a 10% difference or greater.

IV. Discussion

Our experiments demonstrated that the HVJ viral envelope can be radioactively tagged for PET through the coencapsulation of magnetic nanoparticles and optimally sized polycationic agents. We characterized the initial biodistribution of radioactively tagged HVJ-Es and quantitatively evaluated the detected activity *in vivo* in multiple organs in the rat body using PET imaging. Dynamic PET images with control comparisons in combination with histology showed that HVJ-Es primarily accumulate in the liver and spleen as compared to control subjects. We used PET imaging to show that HVJ-Es can be, at least transiently, magnetically targeted to a certain region of the rat body due to the coencapsulation of magnetic nanoparticles. Externally placed, permanent magnets were able to increase the accumulation of HVJ-Es in the head as compared to the nontargeted subjects. These results indicate the potential for magnetically targeted gene and drug delivery to specific parts of the body that can be evaluated *in vivo* and noninvasively using imaging techniques.

The versatility of the HVJ-E makes it a good candidate for the codelivery of therapeutic and imaging agents. In this study, we were able to optimize the encapsulation of ^{18}F-fluoride by coencapsulating magnetic nanoparticles or ferumoxides and cationic polypeptides. Synthetic cationic polypeptides were used based on the hypothesis that they would form an electrostatic bridge between negatively charged ^{18}F-fluoride ions and ferumoxides, forming larger complexes and preventing leakage from the viral membrane. While ferumoxides or cationic agents of certain molecular weights can individually increase the encapsulation efficiency of ^{18}F-fluoride, the inclusion of both ferumoxides and cationic agents results in the greatest increase (Fig. 1). Dextran-coated ferumoxides, which have an iron oxide core, likely have a slight negative charge due to the carboxylic groups of the dextran coating [21]. Cationic agents such as Lipofectamine 2000, a mixture of positively charged and neutral lipids, and PLL molecules, positively charged polypeptides, are used to form electrostatic complexes with the negatively charged phosphate backbone of deoxyribonucleic acid for cell transfection [22], [23]. PLL is commercially available in a range of molecular weights, enabling a size-mediated selection of electrostatic bridging. The larger sized ^{18}F-fluoride-PLL-ferumoxide complexes

were retained within the viral membrane after the membrane was closed after the removal of the detergent. The methodology of optimization of the encapsulation of ^{18}F-fluoride within HVJ-Es may also be relevant for coencapsulating negatively charged, low molecular weight therapeutics. While we included ferumoxides for the purpose of optimizing the encapsulation of ^{18}F-fluoride and for magnetic targeting, its presence within the envelope also enables multimodality imaging with MRI and histological confirmation through Prussian blue staining.

Both imaging and histological findings implicated the liver as a major organ of clearance for HVJ-Es and ferumoxides. Imaging results showing increased accumulation of HVJ-Es in the liver agreed with histological findings demonstrating iron oxide deposits in the liver. Histology was performed to investigate if activity detected on PET scans was due to ^{18}F-fluoride encapsulated within the viral envelope, or loose radioactivity as a result of leakage or residual ^{18}F-fluoride after washing. The C-FPF group showed iron deposits in histological findings but low levels of activity in PET images. This is likely the result of the inclusion of larger ferumoxide molecules, which have been shown to accumulate in the Kupffer cells of the reticuloendothelial system in the liver [24], but which do not present with radioactivity. For the HVJ-E group, high levels of activity on PET images and iron deposits in histological findings together indicate that iron deposits could not be result of loose ferumoxides alone, and demonstrates the clearance of HVJ-Es by the liver. Hepatic uptake of HVJ-Es and ferumoxides is likely the result of the size-mediated mechanisms of the Kupffer cells of the reticuloendothelial system, and to a lesser extent the endothelial and parenchymal cells [24], [25].

Studies that have investigated the biodistributions of other viral vehicles or viruses support the conclusion that the liver and spleen are the primary organs of clearance for HVJ-Es [26]–[28]. For example, if the liver is temporarily removed from circulation by a physical bypass created by clamping the portal vein, hepatic artery, and bile duct, adenoviral vehicles will remain in the blood circulation for a longer period of time [27]. When the simian immunodeficiency virus was radioactively tagged for radiography and infused into the Rhesus monkey, 29.5% of the detected radiation was found in the liver, 5.4% was found in the lung, and 0.4% was found in the spleen [28]. The biodistribution of intravenously injected HVJ-E liposomes, where purified HVJ was inactivated and fused with the phospholipid liposomes to carry DNA, was investigated in various tissues using polymerase chain reaction (PCR) analysis [26]. PCR detected DNA transfection in the lung, spleen, and, predominantly, the liver after one day. The results of these studies confirm that the liver and the spleen are key organs in lowering the efficiency of delivering therapy to any other part of the body, and these clearance mechanisms must be addressed for intravenous administration.

Apparent discrepancies between our biodistribution patterns and those observed in some previous studies may be due to the differences in study design. The focus of our study was to evaluate the initial biodistirbution of HVJ-Es within 2 h, and not to look at the gene expression of an encapsulated plasmid over longer periods of time. Kaneda *et al*. [29] looked at the intravenous biodistribution of luciferase gene-loaded HVJ-Es by measuring the luciferase activity 24 h after injection. They observed gene expression mostly in the spleen and faintly in the lung, but not in the liver. Two possible reasons for the difference in accumulation in the liver are the time point examined and the fact that for activity to be detected in the earlier study, transfection and protein expression had to occur. In our study, the activity was related to the distribution of vehicle itself, which is not necessarily reflective of final reporter gene expression.

The reticuloendothelial system is not only limited to the liver and spleen but also includes the bone marrow. Clearance of HVJ-Es and larger complexes by the reticuloendothelial system may also take place in the bone marrow, and may therefore affect the activity normalization

of the liver and head performed in this study. This additional clearance would result in an underestimation of the activity in the head and liver since we are dividing by the bone activity. However, the histology performed in this study did not show detectable iron deposits, corresponding ferumoxides encapsulated within HVJ-Es, in the bone or bone marrow (Fig. 5).

In addition to characterizing the initial biodistribution of HVJ-Es, we also wanted to examine whether this biodistribution could be altered by magnetic force. Magnetically targeted carriers have been researched for their potential to deliver toxic drugs, such as chemotherapeutics, to a select area of treatment, leaving healthy tissues unharmed and increasing the effectiveness of a given dose [8], [10], [11]. Morishita *et al*. investigated the transfection efficiency of HVJ-Es after allowing the HVJ-Es to electrostatically associate with maghemite particles *in vitro* and *in vivo* and applying an external magnet, but did not observe any increase in efficiency *in vivo* after a direct injection of HVJ-Es into the liver [13]. The difference in the results as compared to the study presented here is most likely due to the differences in study design, as they employed direct intrahepatic injection, not systemic injection.

The results shown in Figs. 7 and 8 demonstrate the specific areas of increased and decreased radioactivity in the head in the presence of permanent magnets. Activity patterns of decreased activity confirm that results shown in Fig. 7 are not due to coregistration errors, which would present as a rim-like artifact pattern for both increased and decreased activity maps. Theoretical mathematical modeling of the behavior of magnetic particles and carriers in blood vessels has indicated that the orientation of blood vessels relative to the magnet greatly affects the fraction of particles affected by magnetic force, and that the field strength required to target magnetic carriers is of the order of 200–700 mT [9], [30]. The field strength of the magnets used in this study falls within this range for up to 3 mm in depth, and to a circular diameter of 9 mm, and the magnetic flux density falls off quickly with distance [Fig. 6(a)]. Magnetic particle immobilization depends greatly on blood flow within the vessel and distance from the magnet. A secondary mechanism is that in a magnetic field, ferumoxide particles become magnetized, and this may result in the agglomeration of HVJ-Es in proximity into larger ensembles with a slower transit time. These effects require further investigation as to the implications for the delivery of drugs or genes to the head vasculature.

This study demonstrates biodistribution pattern of the HVJ-E viral vehicle using PET imaging after the optimization of the encapsulation of radioactivity and iron oxide nanoparticles. We have shown in this study that the HVJ-E is cleared to the liver and spleen and the accumulation of HVJ-Es in the head can be increased, at least transiently, with permanent magnets. This imaging technique can characterize the quantitative kinetic distribution of gene and drug nanocarriers *in vivo*. Magnetic targeting has implications for improving the efficiency of delivery of genes and drugs to a target organ or body area by means of a noninvasive force.

Acknowledgments

This work was supported in part by the National Institutes of Health/National Center for Research Resources under Grant P51 RR000166. The work of J. F. Flexman was supported by the Natural Science and Engineering Research Council of Canada (NSERC).

References

1. Galanis E, Vile R, Russell SJ. Delivery systems intended for *in vivo* gene therapy of cancer: Targeting and replication competent viral vectors. Crit Rev Oncol Hematol 2001;38:177–192. [PubMed: 11369253]
2. Olasz EB, Lang L, Seidel J, Green MV, Eckelman WC, Katz SI. Fluorine-18 labeled mouse bone marrow-derived dendritic cells can be detected *in vivo* by high resolution projection imaging. J Immunol Methods 2002;260:137–148. [PubMed: 11792384]

3. Nicklin SA, Wu E, Nemerow GR, Baker AH. The influence of adenovirus fiber structure and function on vector development for gene therapy. Mol Ther 2005;12:384–393. [PubMed: 15993650]
4. Nakamura H, Kimura T, Ikegami H, Ogita K, Koyama S, Shimoya K, Tsujie T, Koyama M, Kaneda Y, Murata Y. Highly efficient and minimally invasive *in vivo* gene transfer to the mouse uterus using haemagglutinating virus of Japan (HVJ) envelope vector. Mol Hum Reprod 2003;9:603–609. [PubMed: 12970398]
5. Shimamura M, Morishita R, Endoh M, Oshima K, Aoki M, Waguri S, Uchiyama Y, Kaneda Y. HVJ-envelope vector for gene transfer into central nervous system. Biochem Biophys Res Commun 2003;300:464–471. [PubMed: 12504107]
6. Miyoshi S, Flexman JA, Cross DJ, Maravilla KR, Kim Y, Anzai Y, Oshima J, Minoshima S. Transfection of neuroprogenitor cells with iron nanoparticles for magnetic resonance imaging tracking: Cell viability, differentiation, and intracellular localization. Mol Imag Biol 2005;7:286–295.
7. Ito A, Shinkai M, Honda H, Kobayashi T. Medical application of functionalized magnetic nanoparticles. J Biosci Bioeng 2005;100:1–11. [PubMed: 16233845]
8. Alexiou C, Jurgons R, Schmid RJ, Bergemann C, Henke J, Erhardt W, Huenges E, Parak F. Magnetic drug targeting—Biodistribution of the magnetic carrier and the chemotherapeutic agent mitoxantrone after locoregional cancer treatment. J Drug Target 2003;11:139–149. [PubMed: 13129824]
9. Dobson J. Gene therapy progress and prospects: Magnetic nanoparticle-based gene delivery. Gene Ther 2006;13:283–287. [PubMed: 16462855]
10. Kubo T, Sugita T, Shimose S, Nitta Y, Ikuta Y, Murakami T. Targeted systemic chemotherapy using magnetic liposomes with incorporated adriamycin for osteosarcoma in hamsters. Int J Oncol 2001;18:121–125. [PubMed: 11115548]
11. Leakakos T, Ji C, Lawson G, Peterson C, Goodwin S. Intravesical administration of doxorubicin to swine bladder using magnetically targeted carriers. Cancer Chemother Pharmacol 2003;51:445–450. [PubMed: 12802508]
12. Nobuto H, Sugita T, Kubo T, Shimose S, Yasunaga Y, Murakami T, Ochi M. Evaluation of systemic chemotherapy with magnetic liposomal doxorubicin and a dipole external electromagnet. Int J Cancer 2004;109:627–635. [PubMed: 14991586]
13. Morishita N, Nakagami H, Morishita R, Takeda S, Mishima F, Terazono B, Nishijima S, Kaneda Y, Tanaka N. Magnetic nanoparticles with surface modification enhanced gene delivery of HVJ-E vector. Biochem Biophys Res Commun 2005;334:1121–1126. [PubMed: 16134237]
14. Schiepers C, Nuyts J, Bormans G, Dequeker J, Bouillon R, Mortelmans L, Verbruggen A, De Roo M. Fluoride kinetics of the axial skeleton measured *in vivo* with fluorine-18-fluoride PET. J Nucl Med 1997;38:1970–1976. [PubMed: 9430479]
15. Gambhir SS, Barrio JR, Wu L, Iyer M, Namavari M, Satyamurthy N, Bauer E, Parrish C, MacLaren DC, Borghei AR, Green LA, Sharfstein S, Berk AJ, Cherry SR, Phelps ME, Herschman HR. Imaging of adenoviral-directed herpes simplex virus type 1 thymidine kinase reporter gene expression in mice with radiolabeled ganciclovir. J Nucl Med 1998;39:2003–2011. [PubMed: 9829598]
16. Bengel FM, Anton M, Richter T, Simoes MV, Haubner R, Henke J, Erhardt W, Reder S, Lehner T, Brandau W, Boekstegers P, Nekolla SG, Gansbacher B, Schwaiger M. Noninvasive imaging of transgene expression by use of positron emission tomography in a pig model of myocardial gene transfer. Circulation 2003;108:2127–2133. [PubMed: 14530205]
17. Yang H, Berger F, Tran C, Gambhir SS, Sawyers CL. MicroPET imaging of prostate cancer in LNCAP-SR39TK-GFP mouse xenografts. Prostate 2003;55:39–47. [PubMed: 12640659]
18. Flexman JA, Minoshima S, Kim Y, Miyoshi S, Lewellen BL, Cross DJ. A viral envelope as a vehicle for tracer, drug, and gene delivery. IEEE Eng Med Biol Mag Jul./Aug;2006 25(4):70–75. [PubMed: 16898661]
19. Maes F, Collignon A, Vandermeulen D, Marchal G, Suetens P. Multimodality image registration by maximization of mutual information. IEEE Trans Med Imag Apr;1997 16(2):187–198.
20. Press, WH. Numerical Recipes in C: The Art of Scientific Computing. Cambridge, U.K: Cambridge Univ. Press; 1988.
21. Shen T, Weissleder R, Papisov M, Bogdanov A Jr, Brady TJ. Monocrystalline iron oxide nanocompounds (MION): Physicochemical properties. Magn Reson Med 1993;29:599–604. [PubMed: 8505895]

22. Dalby B, Cates S, Harris A, Ohki EC, Tilkins ML, Price PJ, Ciccarone VC. Advanced transfection with Lipofectamine 2000 reagent: Primary neurons, siRNA, and high-throughput applications. Methods (Duluth) 2004;33:95–103.

23. Kwoh DY, Coffin CC, Lollo CP, Jovenal J, Banaszczyk MG, Mullen P, Phillips A, Amini A, Fabrycki J, Bartholomew RM, Brostoff SW, Carlo DJ. Stabilization of poly-L-lysine/DNA polyplexes for *in vivo* gene delivery to the liver. Biochim Biophys Acta 1999;1444:171–190. [PubMed: 10023051]

24. Okon E, Pouliquen D, Okon P, Kovaleva ZV, Stepanova TP, Lavit SG, Kudryavtsev BN, Jallet P. Biodegradation of magnetite dextran nanoparticles in the rat. A histologic and biophysical study. Lab Invest 1994;71:895–903. [PubMed: 7807971]

25. Ogawara K, Yoshida M, Higaki K, Kimura T, Shiraishi K, Nishikawa M, Takakura Y, Hashida M. Hepatic uptake of polystyrene microspheres in rats: Effect of particle size on intrahepatic distribution. J Control Release 1999;59:15–22. [PubMed: 10210718]

26. Tsuboniwa N, Morishita R, Hirano T, Fujimoto J, Furukawa S, Kikumori M, Okuyama A, Kaneda Y. Safety evaluation of hemagglutinating virus of Japan—Artificial viral envelope liposomes in nonhuman primates. Hum Gene Ther 2001;12:469–487. [PubMed: 11268281]

27. Ye X, Jerebtsova M, Ray PE. Liver bypass significantly increases the transduction efficiency of recombinant adenoviral vectors in the lung, intestine, and kidney. Hum Gene Ther 2000;11:621–627. [PubMed: 10724040]

28. Zhang L, Dailey PJ, Gettie A, Blanchard J, Ho DD. The liver is a major organ for clearing simian immunodeficiency virus in rhesus monkeys. J Virol 2002;76:5271–5273. [PubMed: 11967341]

29. Jiang C, Matsuo H, Koyabu N, Ohtani H, Fujimoto H, Yonemitsu Y, Kaneda Y, Narro M, Tsuruo T, Sawada Y. Transluminal gene transfer into brain capillary endothelial cells *in vivo* with HVJ-liposomes. J Drug Target 2002;10:345–352. [PubMed: 12164383]

30. Grief AD, Richardson G. Mathematical modelling of magnetically targeted drug delivery. J Magn Mater 2005;293:455–463.

Biographies

Jennifer A. Flexman (S'99–M'07) received the B. Eng. degree in electrical engineering from McGill University, Montreal, QC, Canada, and the Ph.D. degree in bioengineering from the University of Washington, Seattle.

She held a Postgraduate Scholarship from the Natural Sciences and Engineering Research Council of Canada (NSERC) at the University of Washington. She was a Microwave Test Engineer at Teradyne, Inc., Boston, MA. In 2007, she was a Christine Mirzayan Science and Technology Policy Graduate Fellow for the University–Industry Demonstration Partnership at the National Academies, Washington, DC. She is currently a Michael Smith Foundation for Health Research Fellow in the Department of Advanced Therapeutics, British Columbia Cancer Research Center in Vancouver, BC, Canada. Her current research interests include the use of molecular imaging techniques such as positron emission tomography (PET) and magnetic resonance imaging (MRI) to study biomarkers and therapeutic efficacy.

Dr. Flexman was the student representative to the Administrative Committee of the IEEE Engineering in Medicine and Biology Society for 2006 and 2007.

Donna J. Cross received the B.S.E. degree in aerospace engineering and the Ph.D. degree in neuroscience from the University of Michigan, Ann Arbor.

She is currently a Postdoctoral Fellow in the Department of Radiology, University of Washington, Seattle. Her current research interests include using imaging techniques such as positron emission tomography and MRI to investigate a variety of neuroscientific questions from basic neurophysiology to neurodegenerative diseases as well as novel therapies and response to therapy.

Barbara L. Lewellen is a Certified Nuclear Medicine Technologist and a Clinical Supervisor in the Department of Radiology, University of Washington Medical Center, Seattle. She is also a Research Scientist at the National Primate Research Center and a Member of the Imaging Research Laboratory in the Department of Radiology, University of Washington, Seattle. Her current research interests include image reconstruction algorithms, imaging instrumentation, and small-animal positron emission tomography.

Sosuke Miyoshi was born in Hiroshima, Japan. He received the Ph.D. degree in molecular biology from the University of Tsukuba, Tsukuba, Japan.

From 2003 to 2005, he was a Visiting Scholar in the Department of Bioengineering, University of Washington, Seattle. He is currently a Research Fellow in the Advanced Technology Platform Laboratory, Drug Discovery Research Division, Astellas Pharma, Inc., Tokyo, Japan. His current research interests include evaluating drug efficacy in animals using *in vivo* molecular imaging techniques such as micro-positron emission tomography (PET), high-resolution MRI, and bioluminescence imaging.

Yongmin Kim (S'78–M'82–SM'87–F'96) received the B.S. degree in electronics engineering from Seoul National University, Seoul, Korea, and the M.S. and Ph.D. degrees in electrical engineering from the University of Wisconsin, Madison.

He is a Professor of bioengineering, a Professor of electrical engineering, and an Adjunct Professor of radiology and computer science and engineering at the University of Washington, Seattle. He has more than 450 publications. His group has more than 70 patents, and 25 commercial licenses have been signed. His research interests are in distributed diagnosis and home healthcare, multimedia algorithms and systems, and medical imaging.

Prof. Kim received the Early Career Achievement Award from the IEEE Engineering in Medicine and Biology Society (EMBS) in 1988 and the 2003 Ho-Am Prize in Engineering. He has been a member of the Editorial Board of the Proceedings of the IEEE, IEEE Transactions on Biomedical Engineering, and IEEE Transactions on Information Technology in Biomedicine. He was the President of the IEEE EMBS for 2005 and 2006.

Satoshi Minoshima received the M.D. and Ph.D. degrees from Chiba University School of Medicine, Chiba, Japan.

He completed radiology residency training and moved to the Division of Nuclear Medicine, Departments of Internal Medicine and Radiology, University of Michigan, Ann Arbor, where he subsequently held a tenured faculty appointment. He is currently a Professor of Radiology and Bioengineering, Vice Chair for Research, Department of Radiology, and the Director of the Neuroimaging and Biotechnology Laboratory at the University of Washington, Seattle. His research interests include investigations of neurodegenerative diseases and other brain disorders using innovative imaging technology. His current research focuses on preclinical stages of Alzheimer's disease, animal models of aging, and technology associated with these investigations.

Dr. Minoshima is the past President of the Brain Imaging Council and Vice Chair for the Neuroscience Track, Annual Meeting at the Society of Nuclear Medicine.

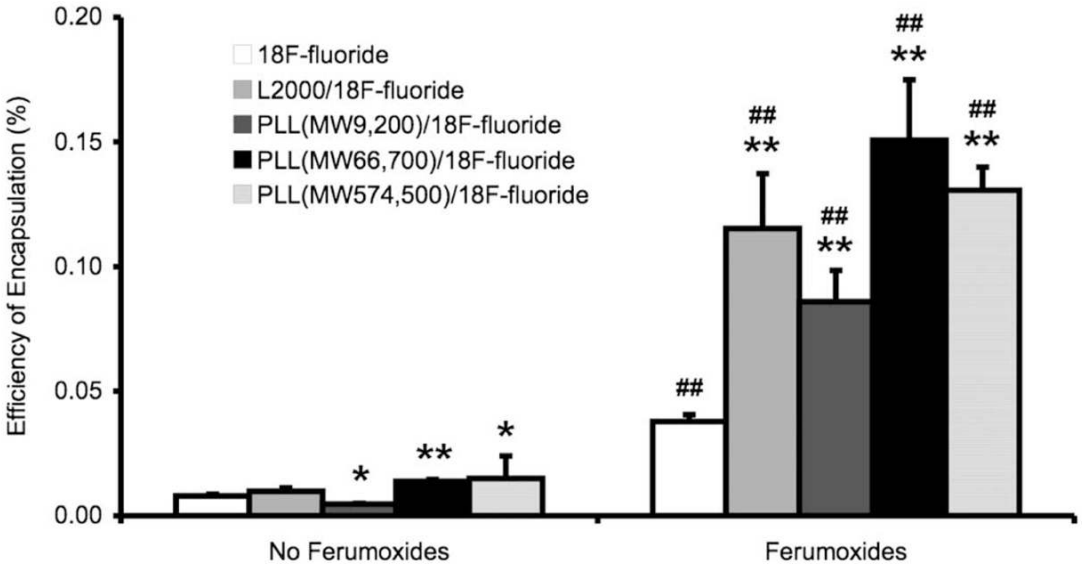

Fig. 1.

Cationic agents and ferumoxides increase the encapsulation efficiency of ^{18}F-fluoride by HVJ-Es. Two stars (**) indicate significance at $p < 0.01$ and one star (*) indicates significance at $p < 0.05$ between ^{18}F-fluoride (white) and ^{18}F-fluoride in combination with cationic agents (Lipofectamine 2000 (L2000) and poly-L-lysine (PLL) of various molecular weights). Two number signs (##) indicate significance at $p < 0.01$ between without ferumoxides and with ferumoxides. Efficiency is determined as a percentage of decay-corrected activity after encapsulation of added radioactivity. (HVJ-E: hemagglutinating virus of Japan envelopes; MW: molecular weight in Dalton).

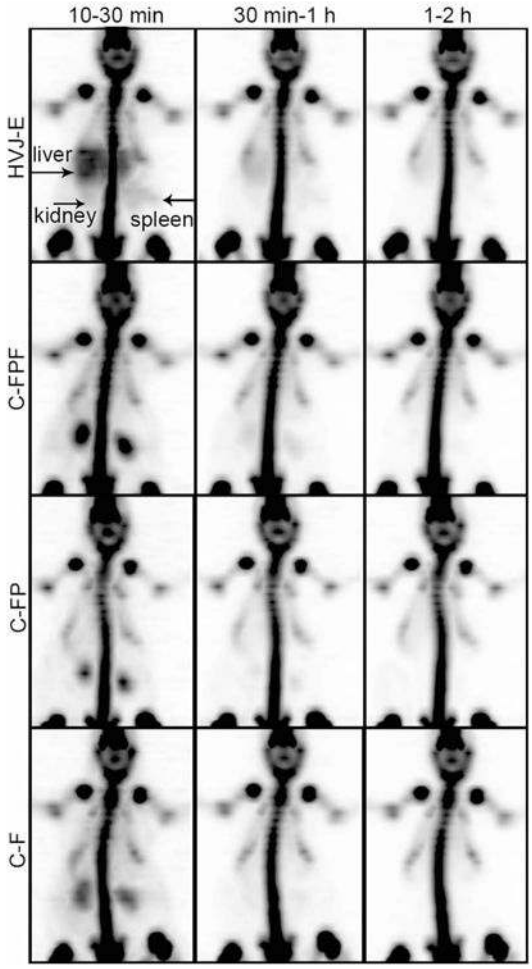

Fig. 2.

Coronal PET image projections of average, normalized activity in the whole rat body. Each image shows the average activity distribution over the time period specified (10–30 min, 30 min–1 h, and 1–2 h) after normalization to steady-state bone activity. PET images of representative subjects from each group show an accumulation of activity in the bone as early as 30 min in all subjects, but early liver and spleen uptake over time is observed only in HVJ-E subjects (arrow). Uptake in the kidneys is lower for HVJ-E subjects, but is shown for all groups predominantly in the earliest time interval. (C-F: control of ^{18}F-fluoride; C-FP: control of PLL and ^{18}F-fluoride; C-FPF: control of ^{18}F-fluoride, PLL, and ferumoxides; HVJ-E: hemagglutinating virus of Japan envelopes encapsulating ^{18}F-fluoride, PLL, and ferumoxides.)

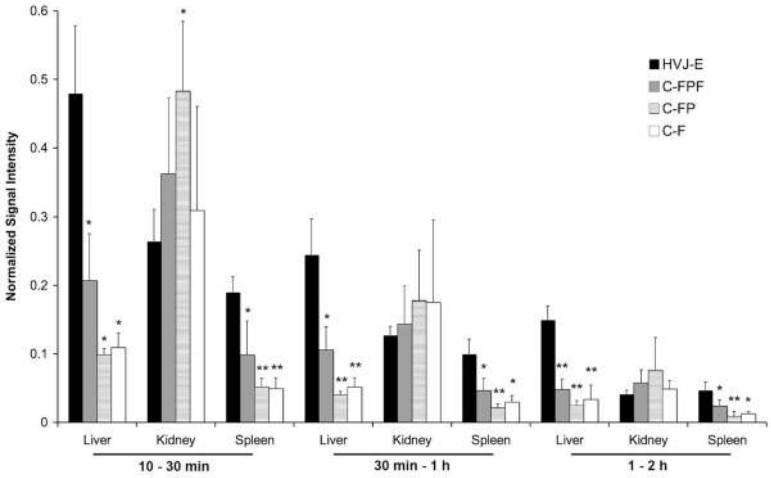

Fig. 3.

Average normalized signal intensity in the liver, kidney, and spleen over three time intervals. Normalized activity was significantly greater in the liver and spleen for the HVJ-E group as compared to all control groups over all time intervals. Normalized activity was significantly greater in the C-FP group as compared to the HVJ-E group in the kidneys from 10 to 30 min, but no other significant differences were observed for the kidneys. One star (*) indicates significance at $p < 0.05$ and two stars (**) indicate significance at $p < 0.01$ as compared to HVJ-E. (C-F: control of ^{18}F-fluoride; C-FP: control of PLL and ^{18}F-fluoride; C-FPF: control of ^{18}F-fluoride, PLL, and ferumoxides; HVJ-E: hemagglutinating virus of Japan envelopes encapsulating ^{18}F-fluoride, PLL, and ferumoxides.)

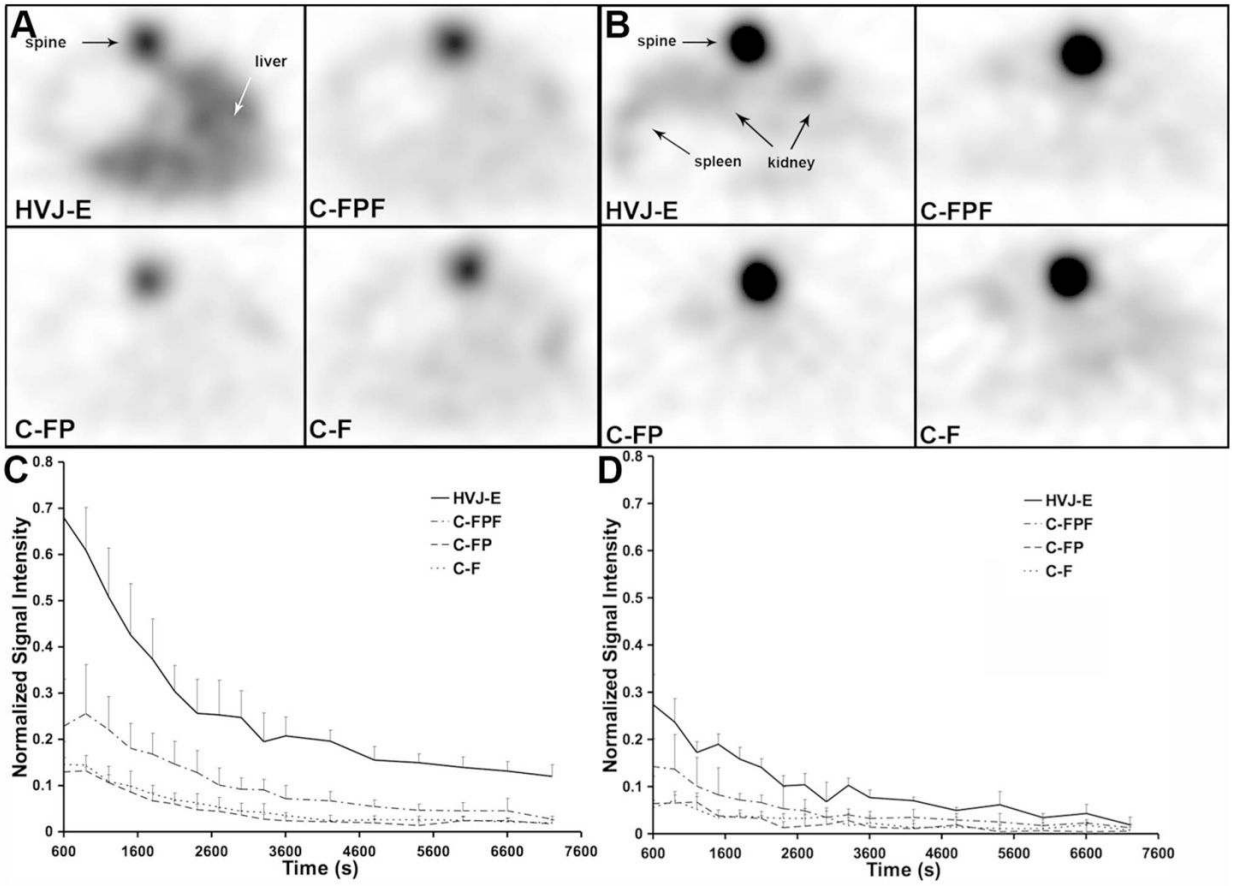

Fig. 4.

Transaxial PET images and activity patterns demonstrate increased uptake of HVJ-Es in the liver as compared to all control subjects. Transaxial, single-slice PET images of representative subjects demonstrating average activity from 10 to 30 min show that greater activity was detected in the (a) liver and (b) spleen for HVJ-E subjects as compared to all control subjects. The dynamic normalized signal intensity in the (c) liver and (d) spleen remained higher for HVJ-E subjects for all time points and decreased with time. (C-F: control of ^{18}F-fluoride; C-FP: control of PLL and ^{18}F-fluoride; C-FPF: control of ^{18}F-fluoride, PLL, and ferumoxides; HVJ-E: hemagglutinating virus of Japan envelopes encapsulating ^{18}F-fluoride, PLL, and ferumoxides.)

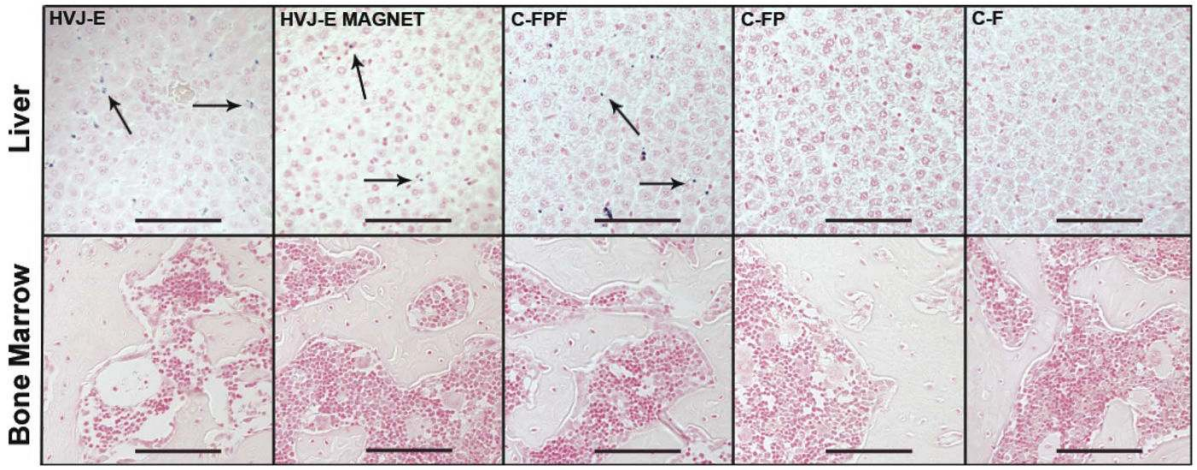

Fig. 5.

Histological staining demonstrates HVJ-Es accumulate in the liver but not in the bone marrow. Prussian blue staining with nuclear fast red counterstaining revealed iron deposits, as indicated by the black arrows, corresponding to ferumoxide particles for HVJ-E, HVJ-E MAGNET, and C-FPF subjects. Iron deposits were not detected in the bone or bone marrow for any treatment group. From left to right, representative microscopic images of the liver and the bone tissue samples are shown for HVJ-E, HVJ-E MAGNET, C-FPF, C-FP, and C-F. Scale bars are 100 μm. (C-F: control of ^{18}F-fluoride; C-FP: control of PLL, and ^{18}F-fluoride; C-FPF: control of ^{18}F-fluoride, PLL and ferumoxides; HVJ-E: hemagglutinating virus of Japan envelopes encapsulating ^{18}F-fluoride, PLL, and ferumoxides.)

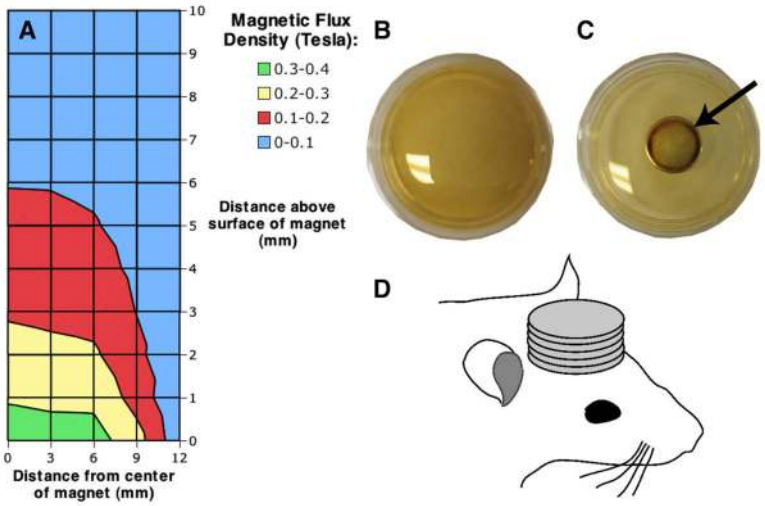

Fig. 6.

Ferumoxide particles are attracted to permanent magnets. (a) Magnetic flux density (in tesla) of five permanent, neodymium magnets is plotted from the center of the magnets. (b) Ferumoxide particles (Feridex IV; Berlex Laboratories, Wayne, NJ) suspended in phosphate-buffered saline are shown in a polystyrene dish. (c) After 1 h aggregated ferumoxide particles placed directly above the magnets are visible as a dark ring around the inner circumference as indicated by the black arrow. (d) During PET scanning, rat subjects had five permanent magnets fixed to the top of the head.

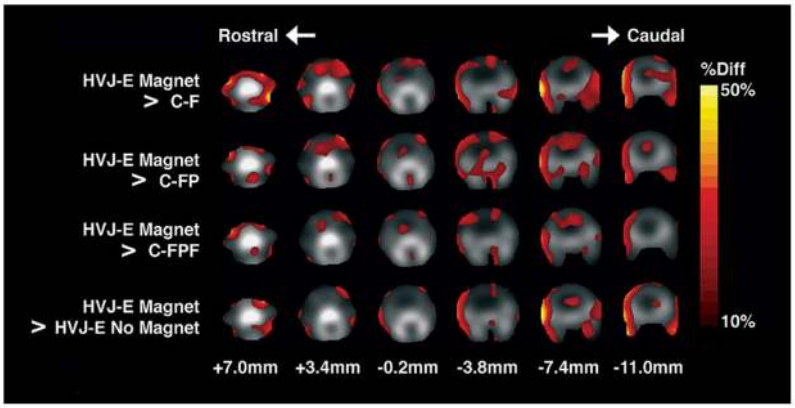

Fig. 7.

Areas of increased activity in the head of magnetically targeted HVJ-Es as compared to the control groups and nontargeted HVJ-Es. The percent difference (% diff) reflecting an increase in the activity is superimposed according to the color scale bar on grayscale images of the head of the rat after coregistration. In the grayscale component of the image, bone structures such as the skull are seen as bright corresponding to the increased activity due to free ^{18}F-fluoride accumulation. Slice level is indicated in millimeters from bregma. (C-F: control of ^{18}F-fluoride; C-FP: control of PLL and ^{18}F-fluoride; C-FPF: control of ^{18}F-fluoride, PLL, and ferumoxides; HVJ-E: hemagglutinating virus of Japan envelopes encapsulating ^{18}F-fluoride, PLL, and ferumoxides.)

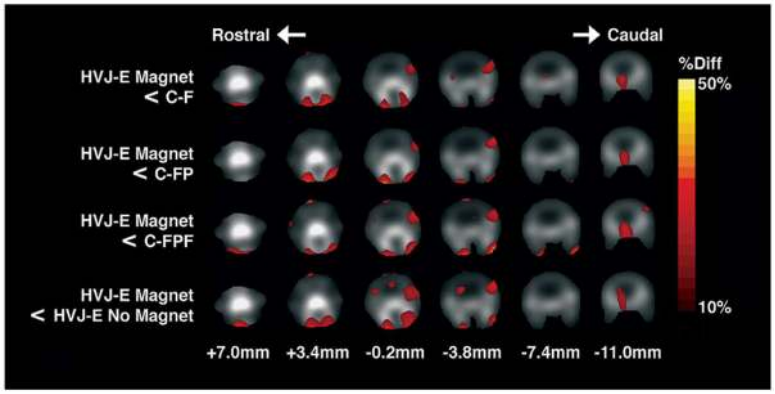

Fig. 8.

Areas of decreased activity in the head of magnetically targeted HVJ-Es as compared to the control groups and nontargeted HVJ-Es. The percent difference (% diff) reflecting a decrease in the activity is superimposed according to the color scale bar on grayscale images of the head of the rat after coregistration. In the grayscale component of the image, bone structures such as the skull are seen as bright corresponding to the increased activity due to free ^{18}F-fluoride accumulation. Slice level is indicated in millimeters from bregma. (C-F: control of ^{18}F-fluoride; C-FP: control of PLL and ^{18}F-fluoride; C-FPF: control of ^{18}F-fluoride, PLL and ferumoxides; HVJ-E: hemagglutinating virus of Japan envelopes encapsulating ^{18}F-fluoride, PLL, and ferumoxides.)